Pin-Hole Array Correlation Imaging: Highly Parallel Fluorescence Correlation Spectroscopy

Daniel J. Needleman,* Yangqing Xu, and Timothy J. Mitchison
Department of Systems Biology, Harvard Medical School, Boston, Massachusetts

ABSTRACT   In this work, we describe pin-hole array correlation imaging, a multipoint version of fluorescence correlation spectroscopy, based upon a stationary Nipkow disk and a high-speed electron multiplying charged coupled detector. We characterize the system and test its performance on a variety of samples, including 40 nm colloids, a fluorescent protein complex, a membrane dye, and a fluorescence fusion protein. Our results demonstrate that pin-hole array correlation imaging is capable of simultaneously performing tens or hundreds of fluorescence correlation spectroscopy-style measurements in cells, with sufficient sensitivity and temporal resolution to study the behaviors of membrane-bound and soluble molecules labeled with conventional chemical dyes or fluorescent proteins.

INTRODUCTION

Fluorescence correlation spectroscopy (FCS) is a powerful technique for studying the dynamics of fluorescently labeled molecules. In a standard FCS experiment, a setup with a configuration similar to a laser scanning confocal microscope is used to measure intensity fluctuations from a diffraction limited volume in a sample. The temporal autocorrelation function of these fluctuations is computed and compared to predictions from a model of the physical processes underlying the system's dynamics (1). Although FCS has many applications (2), it has generated particular excitement because it is one of the few techniques capable of quantitatively measuring concentrations, diffusion coefficients, and binding constants of labeled molecules in cells.

One of the limitations of standard implementations of FCS is that the sample is only probed at a single diffraction limited spot. Therefore, studying heterogeneous samples can be difficult because many individual measurements must be carried out at different locations. This drawback is particularly severe in biological applications because the spatial regulation of biochemical activities is crucial for cellular behaviors (3).

A wide variety of methods have been developed to expand the number of spatial locations that can be conveniently probed by fluorescence correlation-based techniques. The conceptually simplest forms of spatially extended FCS use two separate diffraction limited volumes in the same sample (4,5). Alternatively, a single laser beam can be repetitively scanned across the sample in a linear or circular pattern (6,7). Even more spatial locations can be probed using image correlation spectroscopy (ICS), a suite of related techniques based on computing correlation functions from series of images (8). ICS is most frequently implemented with images collected by one- (9) or two-photon (10) laser scanning confocal microscopy, which make use of a point detector and a fast scanning laser, but is limited to studying relatively slow dynamics with a timescale of hundreds of milliseconds.

Recently, a number of groups have carried out ICS type analysis using area detectors, allowing truly parallel data collection. Back-illuminated electron multiplying charge coupled devices (EMCCD) are excellent cameras for such applications because of their high quantum efficiency, high speed, and low noise. EMCCDs have been used in conjunction with standard confocal optics to perform FCS-style measurements (11,12), but it is difficult to create more than a couple of confocal volumes with this method. Sisan et al. (13) showed that tens of thousands of independent locations can be simultaneously probed using an EMCCD with spinning disk confocal microscopy (SDCM) for ICS. A SDCM contains two connected disks, one with an array of microlenses to focus laser light onto the sample, the other with an array of aligned pinholes, which create the confocal volumes (14). These disks are rapidly spun so that an entire confocal image is created and can be imaged with a camera. Two disadvantages of SDCM for ICS applications are: 1), the acquisition speed is limited to ~1000 frames/s by the speed of rotation of the disks, and 2), the pinholes only take up a small area of the disk, so any given pixel on the camera only receives light from the sample for a short fraction of the exposure time. The resulting decrease in measured intensity leads to a lower apparent particle brightness, greatly reducing the signal/noise. This second drawback limited the applicability of SDCM correlation techniques to ~200 nm fluorescent spheres, which where estimated to have a molecular brightness equivalent to 100,000 fluorophores (13). These two disadvantages can be avoided if total internal reflection (TIRF) illumination is used instead of SDCM. ICS performed with TIRF and EMCCDs has been used to measure the diffusion of dye molecules in lipid bilayers (15) and the diffusion of fluorescent proteins in cell membranes (15,16). However, TIRF can only be used to study the dynamics of molecules within a few hundred nanometers from the coverslip, greatly limiting its applicability.

In this article, we show that if a SDCM is prevented from spinning, it can be used in conjunction with high-powered laser excitation and an EMCCD to simultaneously perform tens or hundreds of FCS type measurements on soluble fluorescently labeled proteins in cells. This technique, which we call pin-hole array correlation imaging (PACI), is an intermediate between FCS and ICS: the time resolution of PACI is 10 to 100 times slower then FCS performed with point detectors, but there is a concurrent increase in the number of spatial locations probed. Conversely PACI interrogates fewer points then is possible with SDCM ICS, but has an increased speed and sensitivity. Unlike TIRF, PACI can be used to investigate the dynamics of molecules away from the coverslip. Although the imaging speed used in the current implementation of PACI is not fast enough to measure the diffusion of free dye molecules in water, we demonstrate its utility on a variety of samples including 40 nm fluorescent colloids, R-Phycoerythrin (a protein complex), a fluorescent dye incorporated into cell membranes, and a soluble fluorescent protein in cells. We believe that PACI has considerable promise as a tool for cell biology, because it is capable of measuring the concentration and diffusion coefficients of chemically and genetically labeled soluble proteins at tens or hundreds of points in cells; and it is easily implemented.

MATERIALS AND METHODS

PACI

A schematic of the experimental system is depicted in Fig. 1. Measurements were performed on a Nikon TE2000 inverted microscope with a Yokogawa (Tokyo, Japan) CSU10 spinning disk confocal head and an EMCCD (iXon 860, Andor (Belfast, Northern Ireland), with 128×128 pixels). A $100\times$ oil immersion objective (1.4 NA) was used. The imaging depth was normally within 5 microns from the coverslip.

An 80 mW, 491 nm solid state laser (Cobolt Calypso 100) and a 60 mW, 560 nm solid state laser (Cobolot Jive 75) were directed to a NEOS acoustic optical tunable filter (AOTF) that was controlled using the Metamorph software package (Molecular Devices, Dowingtown, PA). The total power at the sample ranged from 1.5 mW to 200 μW, depending on the sample under investigation. This power output was spit over ~1000 pinholes, resulting in 1.5–0.2 μW per location. This laser power per pinhole is quite low compared to values typically used in FCS experiments (17), and little bleaching was observed, as determined by a lack of decrease in particle number or average intensity during measurements (data not shown).

The optical setup is similar to that used for imaging applications of SDCM (18), with two modifications: 1), In the CSU10, a safety shutter normally prevents laser excitation when the motor is not spinning. Yokogawa kindly provided a custom-built switch that enabled the motor to be turned on and off while the safety shutter is open. Alternatively, the laser shutter can be disabled by manually removing the shutter or it can be overridden with the pin controller. Although similar procedures could be used for the CSU22, they are not necessary for the CSU-X1. The shutter in the CSU-X1 stays open when the unit is turned off, so simply tuning off the unit is all that is required. 2), The sensor in the iXon 860 is only ~3 mm $\times$ ~3 mm enabling a maximum of ~100 pinholes to be imaged. Demagnifying optics, with a net $0.67\times$ or $0.35\times$, were placed between the EMCCD and the spinning disk confocal head allowing hundreds of additional pinholes to be imaged.

The EMCCD was controlled with Andor's SOLIS software package. The sensor was cooled to $-80°C$. The maximum gain was selected that did not result in saturation, and the baseline clamp was always enabled. Exposure time varied from 0.3 ms to 1.98 ms, depending on the size of the region of interest (and thus the number of pinholes). With full frames, more than 600 individual pinholes could be acquired at a speed of ~500 frames/s. Imaging speed increases with decreasing number of horizontal rows read out, and ~100 pinholes could be investigated at ~1500 Hz and ~10 pinholes at ~3300 Hz. Greater speeds can also be achieved by binning, but this was not normally used. Movies 40,000 frames long were streamed to RAM or a RAID array. Typically, 3–10 movies were taken per sample.
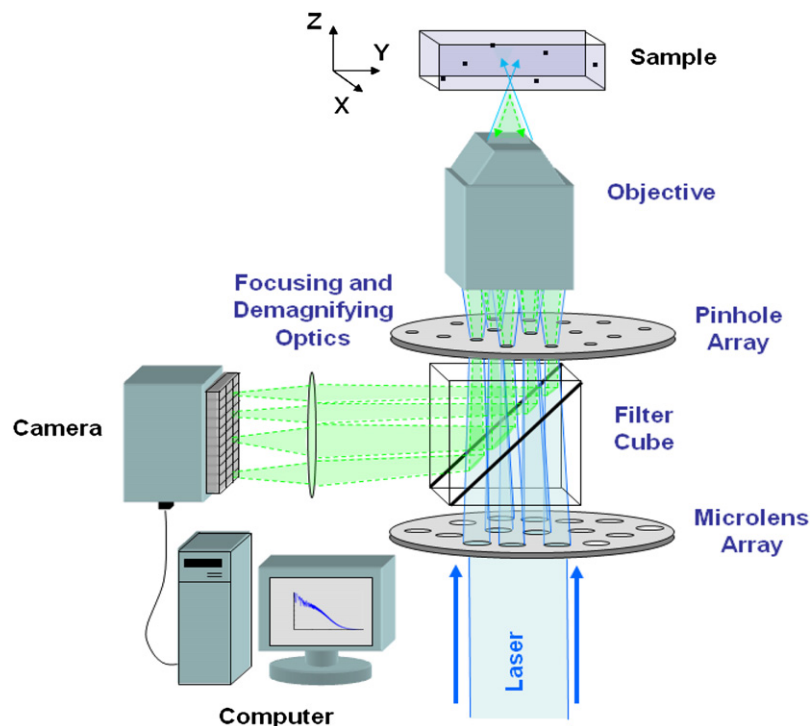

FIGURE 1 Schematic of the experimental setup. The filter cube and microlense and pinhole arrays (which have been modified to allow laser illumination while not rotating) are inside the spinning disk confocal head. Demagnifying optics were placed between the confocal head and the camera to allow more pinholes to be imaged.

Analysis

Images were converted to individual TIFFs and analyzed offline using custom-written MATLAB (The MathWorks, Natick, MA) code. Pictures were loaded and the locations of pinholes were automatically identified using standard particle tracking procedures (19) implemented with freely available MATLAB code (http://physics.georgetown.edu/matlab/). The integrated intensity at each pinhole was calculated by summing over a square 3×3 pixels or 5×5 pixels (depending on the magnification of the optics between the EMCCD and the Nipkow disk). A single, uniform background value was subtracted off, determined by the measured intensity between pinholes, to correct for camera offset and light scattered inside the confocal head. For cell measurements, an intensity threshold was used to select pinholes inside the cell. The threshold was set such that a visual inspection of the selected pinholes coincided with the interior of the cell observed by imaging with the disk spinning. For each investigated pinhole, the 40,000 intensity values per movie were broken into 20 segments, each 2000 points long, and 20 correlation curves were calculated and then averaged together. Correlation curves from pinholes at the same location in separate consecutive movies were averaged together. Total acquisition time was typically between 30 s and 240 s. A nonlinear least-squared curve fit was used to fit the final correlation curves to a model for free diffusion in either three or two dimensions (2D) (see below); with an additional additive constant to correct for small, long timescale changes in intensity. The additive offset was typically two or three orders of magnitude smaller than the amplitude of the correlation curve, but its presence led to significantly improved fits, even though other fit parameters were not sensitive to its exact value. Colloidal aggregates or large, transient movements of cellular structures will produce distorted correlation curves that cannot be fit by the simple models described below. Therefore, we discarded correlation curves where the sum of residuals to the fit exceeded a threshold value. The threshold was set such that only grossly anomalous curves were rejected. The number of curves rejected by this criterion varied depending on the type of sample under investigation, but was never more than 10% of all measured curves, and was often far less than that.

In an FCS type measurement, the autocorrelation function of intensity fluctuations is computed and is given by (20): $\frac{\langle (I(t) - \langle I \rangle)(I(t+\tau) - \langle I \rangle) \rangle}{\langle I \rangle^2} \equiv G(\tau) \propto \int \Phi(\vec{q}) S(\vec{q}, \tau) d\vec{q}$, where $S(\vec{q}, \tau)$ is the dynamic structure factor of the solution, $\Phi(\vec{q})$ is the Fourier transform of the observation volume, $\vec{q}$ is the wave-vector, and τ is the delay time. If the observation volume is approximated as a three-dimensional (3D) Gaussian, then for noninteracting particles diffusion in 3D:

$$G(\tau) = \frac{1}{N}\left(1 + \frac{\tau}{\tau_D}\right)^{-1}\left(1 + \frac{1}{S}\frac{\tau}{\tau_D}\right)^{-\frac{1}{2}}, \qquad (1)$$

whereas for noninteracting particles diffusing in 2D,

$$G(t) = \frac{1}{N}\left(1 + \frac{\tau}{\tau_D}\right)^{-1}, \qquad (2)$$

N is the average number of particles in the observation volume, τ_D, the diffusion time, is the typical time it takes a particle to diffuse out of the observation volume in the plane of focus, and S is a parameter that measures the elongation of the observation volume along the axial direction: $S = (w_z/w_{xy})^2$ where w_{xy} is the $1/e^2$ width of the Gaussian observation volume in the XY (focal) plane and w_z is the width of the observation volume in Z (axial) direction (Fig. 1). Furthermore, $\tau_D = w_{xy}^2/4D$, where D is the diffusion coefficient of the particle. The brightness of particles was measured by dividing the average intensity at a location by the average number of particles at that location.

FCS

Single-point FCS experiments were performed on a custom-built setup. The system was constructed around an inverted microscope (Axioinvert 135

invert TV, Zeiss, Oberkochem, Germany), and a $40\times$ water immersion objective (1.2 NA) was used in all experiments. The excitation light source was the 488 nm or 568 nm line of an Argon-Krypton mixed gas laser (Mells Griot, Carlsbad, CA, 35 LTL 835-208). The emission light was split into two beams, which were separately collected by two Avalanche Photodiodes (APD, Pacer Inc., SPCM-AQR-15). The detection apertures were under filled, resulting in an increased observation volume. The output signals where cross-correlated using a dual-channel correlator (Flex-02-12D/B, Correlator.com, Bridgewater, NJ). This collection procedure results in an autocorrelation curve free from the after-pulsing artifacts, which contaminate single APD measurements.

Depending on the type of fluorophore used, the typical excitation power at the sample was in the range of 10 ~100 μW. The total photon number received by a single APD was typically 1 ~2 kps. Each sample was measured at least three times, with each individual measurement lasting 15–30 s. As in the PACI experiments, correlation curves were fit, using a nonlinear least-squared method, to a model for free diffusion plus an additional additive constant. The system was calibrated with Alexa 488 or Alexa 568, assuming diffusion coefficients of 400 μm^2/s (21). A diffusion coefficient for free dye of 400 μm^2/s is higher than the typically assumed value of 300 μm^2/s, but it seems more consistent with recent measurements (21). Errors in the diffusion coefficient used for the calibration will lead to systematic errors in the reported measurements. Using the older diffusion coefficient as a standard, the observation volume was typically determined to be ~1 femtolitre, with $w_{xy} \sim 0.3$ μm and $w_z \sim 1.5$ μm. The resulting correlation curves were fit using custom-written MATLAB code.

Sample preparation

Colloid solutions were cleaned of aggregates by three rounds of sonication, ~10 min each, and 5 min of centrifugation in a mini centrifuge (National Labnet C-1200). Experiments on colloids and R-Phycoerythrin (RPE) solutions where performed in Lab-Tek II Chambers (No. 1.5 cover glass, 155409), which where blocked with 10 mg/ml BSA for 30 min before use.

DiI was incubated with U2OS cells for ~5 min, cell were rinsed to remove excess dye, and imaged immediately. PTEN null 786-O renal cancer cells constitutively expressing an eGFP-FOXO1A fusion where used for the FOXO-GFP experiments. Cells were kept at 37 C by a custom-built chamber heating and imaged in phenol red free media.

RESULTS AND DISCUSSION

For imaging applications using a spinning disk confocal microscope, the pinhole and microlens arrays are rotated at ~1000 frames/s, so the confocal volumes are scanned over the sample multiple times while a single frame is being acquired. Because the pinholes only take up a small fraction of the area of the disk, a given pixel on the camera does not receive light during the majority of time that an image is being acquired. Thus, stopping the disk from rotating should result in a large increase in the maximum measured intensity. This effect is illustrated in Fig. 2, which compares images taken from a homogeneous sample with the disk rotating and stationary. We calculated the integrated intensity at each pinhole by summing over a square 3×3 pixels. The mean intensity of pinholes with the disk stopped is 4067 (after background subtraction), compared to a mean intensity of 297 (after background subtraction) for similar sized regions with the disk spinning. Therefore, the detected intensity goes up by a factor of 13.7 when the disk is stopped, and a similar increase in measured molecular brightness should

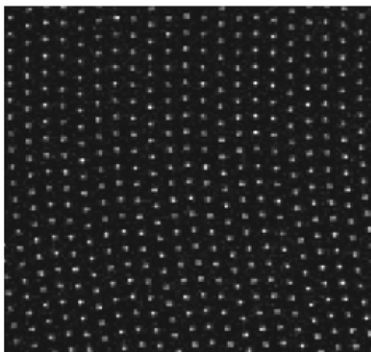## Disk Spinning
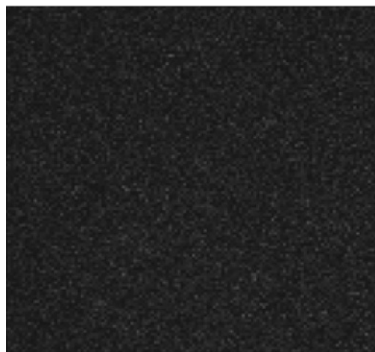
Disk Stationary

FIGURE 2 Solution with Alexa 488 (100 nM) imaged with the Nipkow disk spinning (*left*) and stationary (*right*). The same laser power, camera settings, and gray scale were used in both pictures, illustrating the higher measured intensities when the disk is stopped (see text). The exposure time was 30 ms.

result, greatly facilitating a correlation analysis. We used the PACI setup with a stationary Nipkow disk to perform FCS style measurements.

Measurements on R-Phycoerythrin and colloids

We first sought to quantify the variability between measurements performed through different pinholes in the spinning disk. We investigated the behavior of RPE in 32% sucrose. RPE is a 250 kD, photosynthetic antenna pigment from red algae, which is commonly used as a label in FACS and flow cytometry because it is stable, water soluble, and extremely bright (22). The RPE solution is homogeneous, so an ideal measurement would yield identical values of τ_D and N at each pinhole location; however, differing values are obtained in practice. These deviations arise from two sources: 1), intrinsic differences between locations due to imperfections in the experimental setup, and 2), statistical errors in estimating parameters due to the finite time of a measurement. The statistical errors are reduced as the measurement time increases, with a variance inversely proportional to time, whereas the intrinsic errors are unaffected by increasing the acquisition time. Therefore, we determined the intrinsic differences between pinholes by measuring how the variance in τ_D and N changed with acqui-

sition times. Fig. 3 *A* compares correlation curves acquired in 3.8 s (*left*) to curves acquired in 19 s (*right*). The curves acquired in 19 s are smoother, and the variation between them is smaller. The reduced variation with longer acquisition time can be easily observed by examining the spread in the correlation curves at the shortest lag-time, which is substantially wider for the data acquired in 3.8 s. Fig. 3 *B* depicts the variance (normalized by the mean squared) of τ_D and N as a function of acquisition time and shows fits to the function: $a/T + E$; where T is the measurement time, E is the intrinsic variance between pinholes, and a is a constant (Fig. 3). Taking the square root of E in the two cases reveals that τ_D varies by ~5% between pinholes, whereas N varies by ~7%. These small values indicate that the pinholes are quite uniform.

We attempted to identify other potential sources of systematic error by looking for spatial patterns in results from different pinholes. Fig. 4 shows color-coded maps indicating the spatial distribution of values of N, τ_D, and particle brightness, at different locations from a solution of 40 nm colloids (obtained by fitting the measured correlation curves to Eq. 1). There is no obvious pattern in the distribution of values of τ_D, whereas N seems to have a tendency to slightly increase toward the periphery (Fig. 4). However, the small intrinsic variability of N and τ_D (described above) indicate
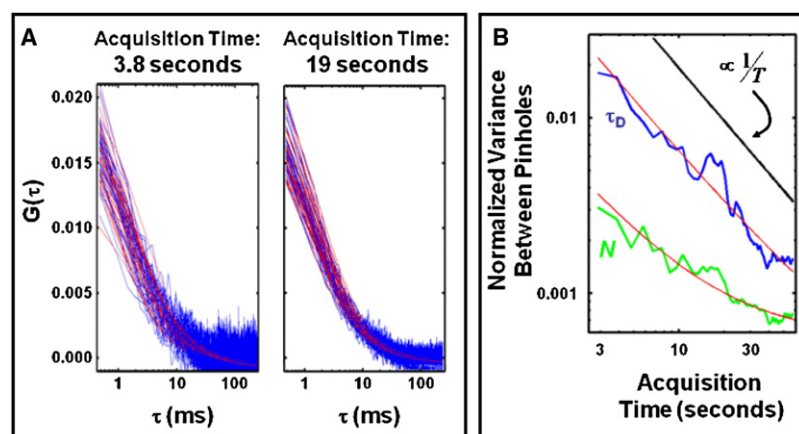

FIGURE 3 Measurements on a solution of RPE in 32% sucrose. (*A*, *left*) 40 correlation curves measured from different pinholes in 3.8 s (*blue*), with associated best fits (*red*). (*A*, *right*) correlation curves from the same 40 pinhole locations measured in 19 s (*blue*), with associated best fits (*red*). (*B*) The variance between pinholes (divided by the mean squared) of measured particle number (N, *green*) and diffusion time (τ_D, *blue*) as a function of acquisition time. Both curves where fit to the function $a/T + E$ (*red*), where E is the intrinsic variance between pinholes, T is the acquisition time, and a is a constant (see text for details).
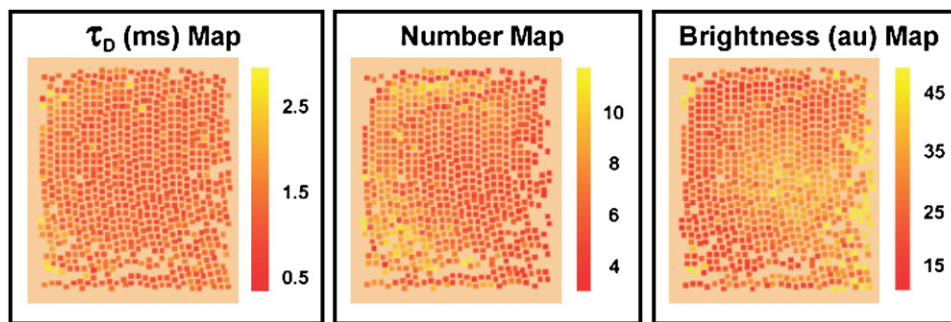
FIGURE 4 Color-scale maps showing the values of diffusion time (*left*, with scale in ms), particle number (*center*), and particle brightness (*right*, with scale in arbitrary units), at different locations in a homogeneous solution of 40 nm colloids.

that any spatial pattern in these parameters is of minor importance. In contrast, the particle brightness is both significantly more variable, with a normalized standard deviation of 23%, and shows a clear spatial structure (Fig. 4, *right*). These observations are consistent with the pinholes, optics, and alignment being spatially uniform, but an inhomogeneous laser illumination causing the variability in particle brightness. Therefore, care must be taken when attempting to use PACI to measure particle brightness, but results for N and τ_D should not depend on the specific pinhole they are measured through.

The small intrinsic variation between pinholes allows correlation curves obtained at different locations to be averaged when studying homogeneous samples, such as solutions of RPE. Very low noise correlation curves of RPE in sucrose solutions were obtained in ~60 s by such averaging, and the resulting curves were fit to Eq. 1 (Fig. 5 *A*). The model correlation curve provided a good fit to the data because of the limited timescales probed, despite the complex photophysical properties of RPE (23) (data not shown). The viscosity of these sucrose solutions of known concentration was determined from standardized tables (24), and Fig. 5 *B* shows that the measured τ_D increases linearly with solution viscosity. This result is expected from the definition of τ_D ($\tau_D \propto D^{-1}$, see above), and the Stokes-Einstein relation, which gives $D \propto \eta^{-1}$, where η is the solution viscosity. Combing data from all solutions of RPE, correcting for the differing viscosities, and using a diffusion coefficient of 39 μm^2/s for RPE in the absence sucrose (measured by FCS, data not shown), yields $w_{xy} = 0.211 \pm 0.014$ μm. Because we used a comparison with FCS to determine w_{xy}, errors in calibrating the FCS setup will give rise to

a bias; thus, if the diffusion coefficient of Alexa 488 is taken to be 300 μm^2/s, instead of the recently suggested value of ~400 μm^2/s (21), a value of $w_{xy} = 0.182 \pm 0.012$ μm results.

We attempted to use fluorescent colloidal particles with nominal diameter of 100 nm as an additional standard. We performed dynamic light scattering measurements on these colloids to more precisely measure their size, revealing that their radius of hydration was $r_h = 59 \pm 8.5$ nm corresponding to a diffusion coefficient of $D = 3.7 \pm 0.54$ μm^2/s. PACI was used to obtain correlation curves from a solution of these colloids, which were averaged over pinholes and fit to a model of one component free diffusion in 3D to give $\tau_d = 4.45 \pm 0.43$ ms, which implies that $w_{xy} = 0.251 \pm 0.043$ μm. Although this calibration to dynamic light scattering data yields a slightly different value of w_{xy} than was obtained by comparison to FCS measurements, they are similar within experimental error. The calibration with dynamic light scattering gives a closer correspondence to the FCS calibration if the diffusion coefficient of small dyes is taken to be 400 μm^2/s. Throughout the rest of the text we assume a value of $w_{xy} = 0.211$ μm, but this must be interpreted with caution. Ultimately, the presented measurements are most reliable for relative changes because systematic errors in w_{xy} are difficult to totally correct for (as in standard FCS) (21); accurate calibrations are required to convert values of τ_D and N to absolute measures of diffusion coefficients and concentrations.

At short lag times, a small but consistent deviation between Eq. 1 and the correlation curves for RPE are evident in Fig. 5 *A*. Although this discrepancy can be accounted for by the known photophysical properties of RPE, which can be modeled as a triplet state with a relaxation times of tens of
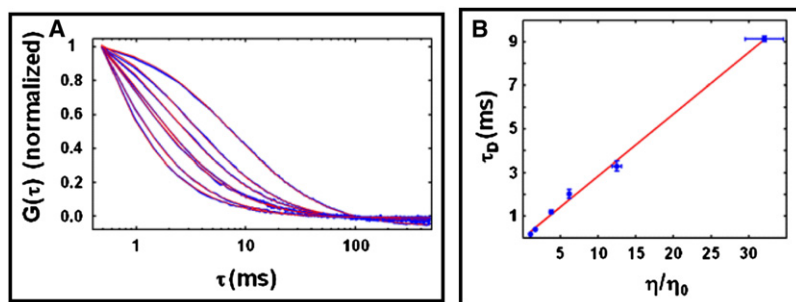

FIGURE 5 PACI measurements obtained by averaging data from different pinholes for solutions of RPE with 0%, 16%, 32%, 40%, 48%, and 56% sucrose. (A) Normalized correlation curves (*blue*) with best fits to Eq. 1 (*red*). (B) As expected, the measured diffusion time, τ_D, increases linearly with the solutions viscosity, η, (where η_0 is the viscosity of water). Viscosities for sucrose solutions were obtained from (24). Errors in viscosity were assumed to arise from a 1% error in determining the sucrose concentration (with a linear extrapolation of the viscosities from (24)).

microseconds ((23) and data not shown), a similar disagreement between measured correlation curves and Eq. 1 can result from an incorrectly aligned optical setup (25). Therefore, we performed additional measurements on a simpler system to better characterize the PACI setup. Fig. 6 A shows data from a solution of 40 nm colloids, obtained in ~5 min by averaging results from ~380 separate pinholes. The resulting $G(\tau)$ can be well fit by Eq. 1 over four orders of magnitude of correlation, indicating that the confocal volume is well approximated by a Gaussian (25). Misalignment resulting in a non-Gaussian volume would result in a significant, systematic disagreement with Eq. 1. We do observe small, nonrandom deviations with residuals of order 10^{-3} (Fig. 6 A, lower), which is the magnitude of error expected from approximating the observation volume of a well-aligned confocal systems as a 3D Gaussian instead of using the full result from diffraction theory (25). The fit gives $\tau_D = 2.1$ ms, leading to a measured diffusion coefficient of $5.2 \pm 0.3\ \mu m^2/s$ (assuming $w_{xy} = 0.211\ \mu m$ as described above), which is close to the value of 5.5 $\mu m^2/s$ expected for spheres of this size. A poorly aligned system will result in an apparent divergence of w_z/w_{xy} (25), whereas our fit yields a reasonable value of 5.6.

We performed an additional test of the shape of the observation volume by measuring the volume with two independent methods. Firstly, we estimated the size of the observation volume by our knowledge of w_{xy}, obtained from calibration with FCS, and w_z/w_{xy}, obtained from fitting the shape of the correlation curve; if the observation volume is assumed to be a 3D Gaussian, then we can calculate its volume as $V_{gaus} = \pi^{3/2} w_{xy}^2 w_z = 0.292 \pm 0.034\ \mu m^3$. Secondly, we directly calibrated the observation volume by measuring the average number of colloidal particles at various dilutions with FCS and PACI (Fig. 6 B). Measurements on free dye of known concentration reveal that the FCS volume was $1.65 \pm 0.29\ \mu m^3$, whereas the experiments with colloids indicate that the PACI volume is $52\% \pm 20\%$ of the FCS volume: resulting in an observation volume of $0.85 \pm 0.39\ \mu m^3$ for PACI. This directly measured volume is significantly larger than volume calculated assuming

a 3D Gaussian shape. The apparent discrepancy is most likely caused by the actual shape of the observation volume in a Nipkow disk microscope; a careful theoretical and experimental study has demonstrated that the volume is a Gaussian with long tails, caused by cross-talk between separate pinholes (26). Such long tails would not be expected to contribute to the shape of the correlation function, which is dominated by the fluctuations from particles moving around the central Gaussian portion, but would result in an effectively larger observation volume as is observed.

Measurements of dil in cells

We used PACI to measure the diffusion of diI, a fluorescent lipid analog, in cell membranes to illustrate the ability of this technique to probe biologically relevant dynamics in cells. Data were collected from 44 locations at the edge of a U2OS cell in ~90 s. Fitting the measured correlation curves to Eq. 2 allows τ_D and N to be extracted at each location (Fig. 7 A). The mean τ_D is 4.6 ms, leading to a diffusion coefficient of 2.4 $\mu m^2/s$, similar to values previously reported (27). However, the behavior of diI is highly heterogeneous, and a wide range of τ_D and N were measured in a single cell (Fig. 7 B), in agreement with the large variability that has been observed in the diffusion of membrane bound dyes in tissue culture cell membranes using ICS performed with an EMCCD and TIRF (15).

Measurements of autofluorescent proteins in cells

In the previous sections of this work, we demonstrated that PACI can be used to measure the diffusion of 40 nm colloids, a highly fluorescent protein complex (RPE), and chemically labeled flourophores attached to lipid analogs in cell membranes. In this last section we show that PACI can also be used to characterize the dynamics of soluble proteins in cells.

We used PACI to characterize the diffusion of FOXO, a transcription factor, in PTEN null 786-O renal cancer cells stably expressing an eGFP-FOXO fusion protein. The absence of PTEN in this cell line causes constitutively active Akt to phosphorylate FOXO, leading to a cytoplasmic
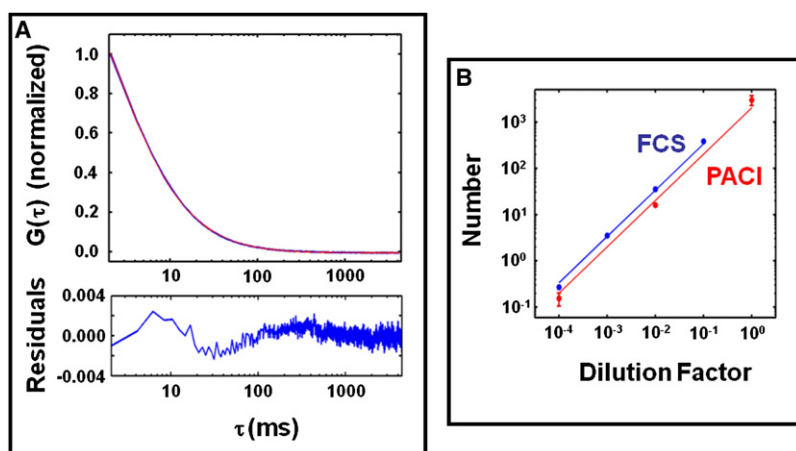

FIGURE 6   (A, upper) A correlation curve from a solution of 40 nm colloids, obtained in 5 min by averaging data from ~380 pinholes (blue) with a best fit to Eq. 1 (red). (A, lower) The residuals to the fit are of order 10^{-3}. (B) A dilution series for 40 nm colloids showing how the measured number of particles changes (FCS in blue, PACI in red). Lines are best fits to the expected linear trend.
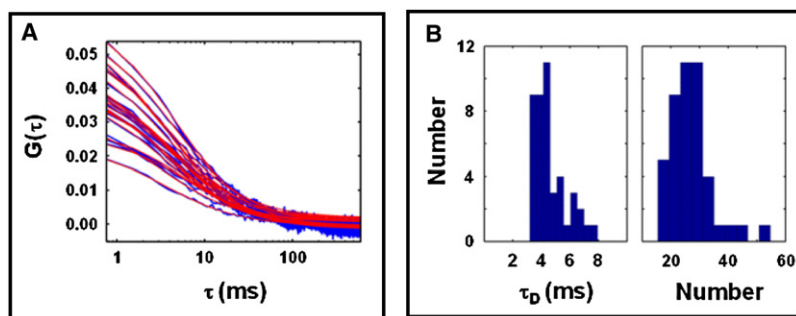
FIGURE 7 Dynamics of labeled diI in the plasma membrane of U2OS cells. (A) 16 representative correlation curves (blue) with best fits to Eq. 2 (red). (B) Histograms of the measured values of diffusion time, (τ_D, left), and particle number (right) obtained from 44 locations in ~90 s.

localization of FOXO under our standard imaging conditions. Fig. 8 A shows 15 (from a total of 89) correlation curves obtained from a single cell in ~161 s. Fitting these data using Eq. 1 gives $\tau_D = 1.8 \pm 0.6$ ms, yielding a diffusion coefficient of $D = 6.1 \pm 2.0$ μm^2/s, comparable to a value of $D \sim 5.2$ μm^2/s obtained from standard FCS measurements on these cells (data not shown). This low diffusion coefficient is potentially indicative of FOXO being part of a large complex or engaging in transient interactions with cellular structures. A wide range of τ_D and N were measured within a single cell (Fig. 8 B). This variability of ~33% (standard deviation/mean) in τ_D and ~24% in N is far greater than can be accounted by artifacts caused by the intrinsic discrepancies between pinholes (see above), and therefore these results are caused by true differences in the behavior of FOXO at different locations in the cell. The measured variation might be caused by changes in underlying cytoskeletal or membrane structures, but more experiments will be required to test that hypothesis.

In most cells, there was no obvious pattern to this heterogeneity (Fig. 8 C). However, on occasion, spatial trends were visible. Fig. 9 shows one such example where the measured number of particles gradually decreases toward the edge of the cell. It is not clear what gives rise to this pattern, but it is possible that it reflects the thinning of the cell. If the cell becomes thinner than the observation volume, then a lower measured average number of particles per pinhole will result, even if the actual concentration is uniform. Still, these data demonstrates the ability of PACI to quantitatively measure spatial patterns in the behaviors of soluble proteins throughout cells.

CONCLUSIONS

In this study, we have shown that an EMCCD can be used in conjunction with a stationary spinning disk confocal microscope to simultaneously perform tens or hundreds of FCS style measurements with enough speed and sensitivity to
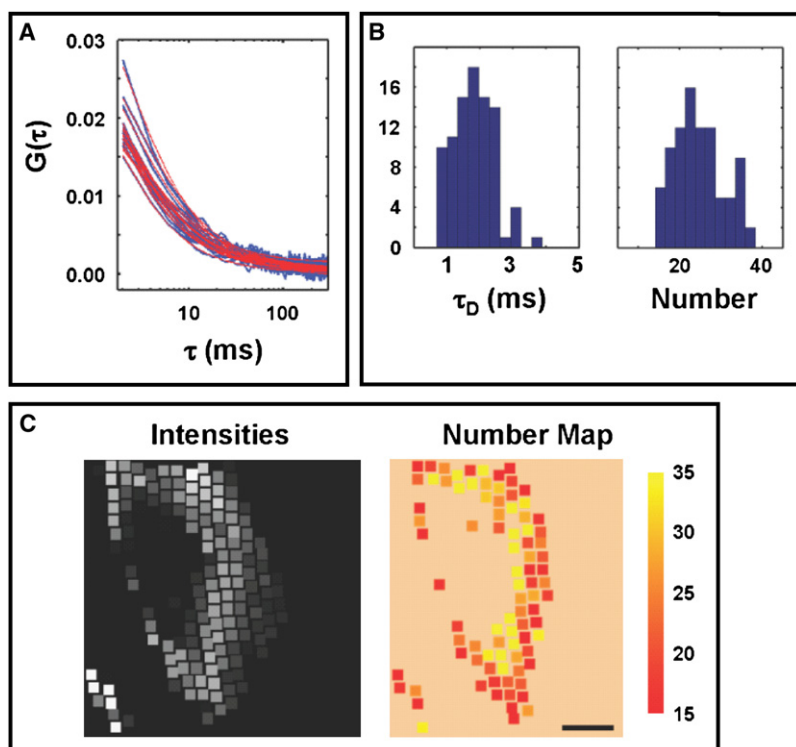

FIGURE 8 Behavior of FOXO-GFP in tissue culture cells studied with PACI. (A) 15 representative correlation curves (blue) with best fits to Eq. 1 (red). (B) Histograms of the measured values of diffusion time, (τ_D, left), and particle number (right) obtained from 89 locations in ~161 s. (C) Spatial maps showing the measured mean fluorescence intensity (left) and particle number (right) at different pinholes. The focus is a few microns above the coverslip. Under the experimental conditions FOXO-GFP is predominantly cytoplasmic, and consistent correlation curves could not be obtained from the nucleus. Scale bar = 10 μm.
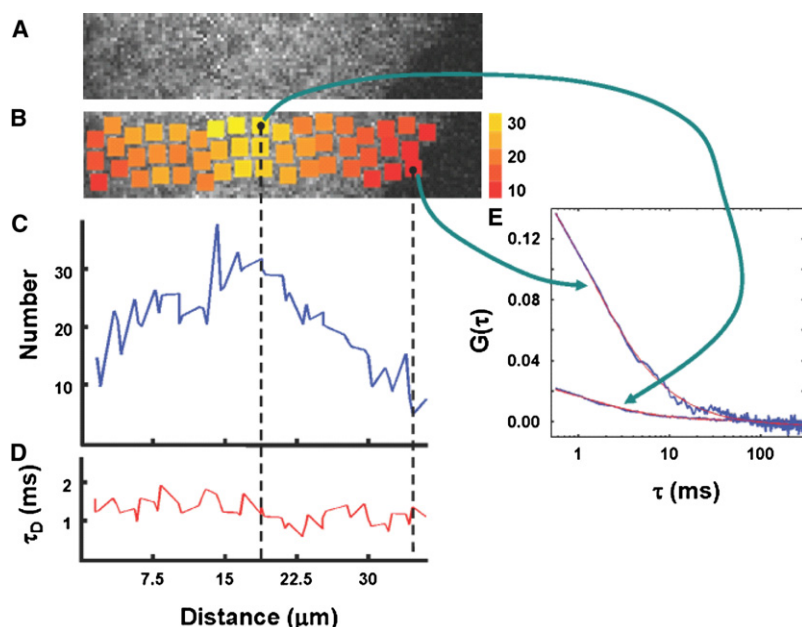
FIGURE 9 FOXO-GFP at the edge of a cell. (*A*) An image of the cell edge obtained with the Nipkow disk spinning. (*B*) The disk was stopped and a PACI measurement was performed. The displayed map shows the locations of the pinholes with their color indicating the measured number of particles at that location (*scale to right*). (*C*) The measured number of particles at each location as a function of distance along the cell. (*D*) The measured diffusion time as a function of distance along the cell. (*E*) Two represented correlation curves from the indicated locations (*blue*) with the associated best fits to Eq. 1 (*red*).

quantify biologically relevant dynamics of membrane and soluble molecules labeled with conventional chemical or genetic fluorphores. This approach, which we call PACI, can be viewed as an intermediate between standard FCS and ICS. PACI has a number of advantages over existing techniques: it can probe timescales hundreds of times faster then is possible with point scanning ICS; the obtained signal/noise is more than 10-fold greater than ICS performed with a rotating Nipkow disk; unlike ICS with TIRF illumination, PACI can be used to measure the dynamics of molecules away from the coverslip. However, the smallest accessible delay time in PACI is far slower than can be achieved with single-point FCS and PACI probes sparser spatial locations then ICS.

There are three factors to consider when deciding whether to use an ICS style analysis with a spinning disk or a PACI style setup with the disk stationary; 1), the timescale of the systems dynamics; 2), the desired spatial resolution; 3), the molecular brightness.

PACI allows faster timescales to be probed because the speed of ICS is limited by the scan rate of the spinning disk. The maximum frame rate that can be achieved with the disk spinning depends on the model of spinning disk and the setup; for the CSU10 and CSUX-1 basic model, the maximum rate is 360 frames/s (or ~30 frames/s if the camera and disk are not synchronized), whereas for the CSU22 1000 frames/s can be acquired and 2000 frames/s can be achieved with the CSUX-1 high-end model. These rates are slower, some substantially slower, than the maximum frame rate of 3300 frames/s used in this study with the disk stationary.

Conversely, ICS permits more spatial locations to be investigated because the spatial resolution of PACI is limited by the fixed spacing between pinholes on the Nipkow disk. The importance of molecular brightness is more subtle, and the relative benefit of the two techniques depends on the characteristics of the sample. Koppel (28), later expanded by Kask et al. (29), analyzed two limiting cases which are helpful to consider; for small molecular brightness, the so-called ''Poisson noise limit'', statistical noise is dominated by the stochastic nature of the emission and detection of photons, whereas in the limit of high-molecular brightness, the ''optimal high-counting-rate limit'', statistical noise is dominated by the number of times molecules move through the observation volume.

In the ''optimal high-counting-rate limit'', the signal/noise of fluorescence correlation measurements are independent of molecular brightness (28,29). Therefore, if particles are already very bright with the disk spinning, increasing brightness even further by stopping the disk will not improve the signal/noise. Therefore, in this limit, PACI is only advantageous if the sampling rate is limited by the disk scan rate.

In the ''Poisson noise limit'', which will be relevant to many studies involving fluorescent fusion proteins, the signal/noise is proportional to the molecular brightness (28,29). Therefore if stopping the disk increases the brightness by a factor of ~14, as we measured, in the limit of low molecular brightness the signal/noise will also increase by a factor of ~14. If the system is at steady-state, the same increase in signal/noise could be obtained even with the disk spinning by simply collecting data for a longer time period. However, the signal/noise increases with the square root of sampling time (28,29), so to obtain a similar ~14-fold increase in signal/noise would require increasing sampling time by a factor of ~196. This would mean increasing the typical measurement time from ~2 min to

~6.5 h, which might not be practical. Another way to improve the signal/noise if the disk is spinning is to average results from different spatial locations (30), but in the ''Poisson noise limit'', spatial averaging does not offset the reduced molecular brightness associated with spinning the disk. This is because spinning the disk effectively divides the excitation laser among multiple spatial locations by time sharing, so if the number of spatial locations that can be probed increases by a factor of N, the brightness of each spot decreases by a factor of N. However, in the ''Poisson noise limit'', the signal/noise is proportional to the molecular brightness (28,29) but only increases like the square root of the number of spatial locations (30). Therefore, spinning the disk and spatially averaging will result in a decrease in signal/noise relative to PACI of $\sqrt{N}$, which from our brightness measurements quoted above we estimate to be $\sqrt{N} \approx \sqrt{14} \approx 3.7$. In summary, ICS is preferable when studying slowly evolving, bright particles with complex spatial structure, such as the cytoskeleton, whereas PACI is preferable when studying dim samples with rapid dynamics, such as soluble proteins in cells.

There are a number of ways in which the described PACI system could be improved. The current implementation of PACI has a minimum time resolution of ~300 μs, significantly worse than standard FCS. However, it should be relatively straightforward to reach a time resolution of ~20 μs, fast enough to measure the diffusion of free dye in water, by covering part of the CCD chip and using the ''fast kinetic'' readout mode, as has been previously done with an EMCCD and confocal illumination (11). It would also be beneficial to combine the describe correlation analysis with an analysis of the measured intensities using methods such as photon-counting histogram (31), or the recently developed N&B approach (32), though these will have to be modified to account for the unique noise characteristics of EMCCDs (33) and the inhomogeneous illumination (see above). Finally, it should be possible to develop a two-color version of PACI, similar to two-color FCS (34), to measure protein binding at multiple locations throughout cells.

REFERENCES

1. Kim, S. A., K. G. Heinze, and P. Schwille. 2007. Fluorescence correlation spectroscopy in living cells. *Nat. Methods.* 4:963–973.

2. Krichevsky, O., and G. Bonnet. 2002. Fluorescence correlation spectroscopy: the technique and its applications. *Rep. Prog. Phys.* 65:251–297.

3. Kholodenko, B. N. 2006. Cell-signaling dynamics in time and space. *Nat. Rev. Mol. Cell Biol.* 7:165–176.

4. Brinkmeier, M., K. Dorre, J. Stephan, and M. Eigen. 1999. Two-beam cross-correlation: a method to characterize transport phenomena in micrometer-sized structures. *Anal. Chem.* 71:609–616.

5. Dittrich, P. S., and P. Schwille. 2002. Spatial two-photon fluorescence cross-correlation spectroscopy for controlling molecular transport in microfluidic structures. *Anal. Chem.* 74:4472–4479.

6. Digman, M. A., C. M. Brown, P. Sengupta, P. W. Wiseman, A. F. Horwitz, and E. Gratton. 2005. Measuring fast dynamics in solutions and cells with a laser scanning microscope. *Biophys. J.* 89:1317–1327.

7. Ruan, Q., M. A. Cheng, M. Lei, E. Gratton, and W. W. Mantulin. 2004. Spatial-temporal studies of membrane dynamics: scanning fluorescence correlation spectroscopy (SFCS). *Biophys. J.* 87:1260–1267.

8. Kolin, D. L., and P. W. Wiseman. 2007. Advances in image correlation spectroscopy: measuring number densities, aggregation states, and dynamics of fluorescently labeled macromolecules in cells. *Cell Biochem. Biophys.* 49:141–164.

9. Peterson, N. O., P. L. Hoddelius, P. W. Wiseman, O. Seger, and K. E. Magnusson. 1993. Quantitation of membrane receptor distributions by image correlation spectroscopy: concept and application. *Biophys. J.* 65:1135–1146.

10. Wiseman, P. W., J. A. Squier, M. H. Ellisman, and K. R. Wilson. 2000. Two-photon video rate image correlation spectroscopy (ICS) and image cross-correlation spectroscopy (ICCS). *J. Microsc.* 200:14–25.

11. Burkhardt, M., and P. Schwille. 2006. Electron multiplying CCD based detection for spatially resolved fluorescence correlation spectroscopy. *Opt. Express.* 14:5013–5020.

12. Kannan, B., J. Y. Har, P. Liu, I. Maruyama, J. L. Ding, and T. Wohland. 2006. Electron multiplying charge-coupled device camera based fluorescence correlation spectroscopy. *Anal. Chem.* 78:3444–3451.

13. Sisan, D. R., R. Arevalo, C. Graves, R. McAllister, and J. S. Urbach. 2006. Spatially resolved fluorescence correlation spectroscopy using a spinning disk confocal microscope. *Biophys. J.* 91:4241–4252.

14. Inoue, S., and T. Inoue. 2002. Direct-view high-speed confocal scanner: the CSU-10. *Methods Cell Biol.* 70:87–127.

15. Kannan, B., L. Guo, T. Sudhaharan, S. Ahmed, I. Maruyama, and T. Wohland. 2007. Spatially resolved total internal reflection fluorescence correlation microscopy using an electron multiplying charge-coupled device camera. *Anal. Chem.* 79:4463–4470.

16. Kolin, D. L., D. Ronis, and P. W. Wiseman. 2006. K-space image correlation spectroscopy: a method for accurate transport measurements independent of fluorophore photophysics. *Biophys. J.* 91:3061–3075.

17. Schwille, P., U. Haupts, S. Maiti, and W. W. Webb. 1999. Molecular dynamic in living cells observed by fluorescence correlation spectroscopy with one- and two-photon excitation. *Biophys. J.* 77:2251–2265.

18. Adams, M. C., W. C. Salmon, S. L. Gupton, C. S. Cohan, T. Wittman, N. Prigozhina, and C. M. Waterman-Storer. 2003. A high-speed multispectral spinning-disk confocal microscope system for fluorescent speckle microscopy of living cells. *Methods.* 29:29–41.

19. Crocker, J. C., and D. G. Grier. 1996. Methods of digital video microscopy for colloidal studies. *J. Colloid Interface Sci.* 179:298–310.

20. Ricka, J., and T. Binkert. 1989. Direct measurement of a distinct correlation function by fluorescence cross correlation. *Phys. Rev. A.* 39:2646–2652.

21. Dertinger, T., V. Pacheco, I. von der Hocht, R. Hartmann, I. Gregor, and J. Enderlein. 2007. Two-focus fluorescence correlation spectroscopy: a new tool for accurate and absolute diffusion measurements. *ChemPhysChem.* 8:433–443.

22. MacColl, R., and D. Guard-Friar. 1987. Phycobiliproteins. CRC Press, Boca Raton, FL.

23. Hwang, L. C., M. Gosch, T. Lasser, and T. Wohland. 2006. Simultaneous multicolor fluorescence cross-correlation spectroscopy to detect higher order molecular interactions using single wavelength laser excitation. *Biophys. J.* 91:715–727.

24. Wolf, A. V., M. G. Brown, and P. G. Prentiss. 1979. Concentration properties of aqueous solutions: conversion tables. *In* CRC Handbook of Chemistry and Physics. D. R. Lide, Editor. CRC: Boca Raton, FL.

25. Hess, S. T., and W. W. Webb. 2002. Focal volume optics and experimental artifacts in confocal fluorescence correlation spectroscopy. *Biophys. J.* 83:2300–2317.

26. Egner, A., V. Andresen, and S. W. Hell. 2002. Comparison of the axial resolution of practical Nipkow-disk confocal fluorescence microscopy with that of multifocal multiphoton microscopy: theory and experiment. *J. Microsc.* 206:24–32.

27. Bacia, K., D. Scherfeld, N. Kahya, and P. Schwille. 2004. Fluorescence correlation spectroscopy related rafts in model and native membranes. *Biophys. J.* 87:1034–1043.

28. Koppel, D. E. 1974. Statistical accuracy in fluorescence correlation spectroscopy. *Phys. Rev. A.* 10:1938–1945.

29. Kask, P., R. Gunther, and P. Axhausen. 1997. Statistical accuracy in fluorescence fluctuation experiments. *Eur. Biophys. J.* 25:163–169.

30. Kolin, D. L., S. Costantino, and P. W. Wiseman. 2006. Sampling effects, noise, and photobleaching in temporal image correlation spectroscopy. *Biophys. J.* 90:628–639.

31. Chen, Y., J. D. Muller, P. T. C. So, and E. Gratton. 1999. The photon counting histogram in fluorescence fluctuation spectroscopy. *Biophys. J.* 77:553–567.

32. Digman, M. A., R. Dalal, A. F. Horwitz, and E. Gratton. 2008. Mapping the number of molecules and brightness in the laser scanning microscope. *Biophys. J.* 94:2320–2332.

33. Robbins, M. S., and B. J. Hadwen. 2003. The noise performance of electron multiplying charge-coupled devices. *IEEE Trans. Electron. Dev.* 50:1227–1232.

34. Hwang, L. C., and T. Wohland. 2007. Recent advances in fluorescence cross-correlation spectroscopy. *Cell Biochem. Biophys.* 49:1–13.